Formation of $n = 2$ positronium from untreated metal surfaces

T. D. Steiger and R. S. Conti

Department of Physics, University of Michigan, Ann Arbor, Michigan 48109

The formation of $n = 2$ positronium is investigated using a positron beam incident on a variety of untreated metal foils and crystals. The maximum measured formation fraction is much higher than any previously reported for such targets. Fully 2% of the incident positrons are observed to form $n = 2$ positronium at low input energy with little dependence upon the metal substrate of the formation surface. The $n = 2$ positronium spectra exhibit lifetime components characteristic of two distinct populations with different kinetic energies. The dependence of each of these components on the incident positron energy is studied and interpreted as being consistent with existing theories of positron interactions with metals. The production of $n = 2$ positronium using positrons transmitted through metal meshes and thin foils is also observed and discussed briefly.

I. INTRODUCTION

Excited-state positronium provides an opportunity to test QED via atomic spectroscopy experiments in the absence of hadronic interactions and nuclear size effects. Although highly excited states have been observed [1], the present discussion is limited to $n = 2$ positronium (Ps*). The production of Ps* has been reported through optical excitation of the ground state [2–4], but it is more common to produce Ps* directly by injecting slow positrons into metal foils [5,6].

This formation method has been used in several measurements of the $n = 2$ positronium fine structure [7–9]. The most precise experiment yields a 300-ppm result [8] which is in reasonable agreement with QED calculations [10] through terms proportional to $\alpha^3 \Re$. However, the current level of experimental precision is comparable to the expected contribution from terms of order $\alpha^4 \Re$, and thus these terms have not been rigorously tested. An experiment has been proposed which will improve the experimental precision to ~ 10–20 ppm [11]. This experiment will definitively test terms of order $\alpha^4 \Re$ — including the recently calculated [12] terms proportional to $\alpha^4 \ln(\alpha^{-1}) \Re$. Such a sensitive test of QED in positronium is of particular interest because of the currently unresolved difference between QED calculations and measurements of the orthopositronium (o-Ps) decay rate [13,14].

Previous Ps* fine-structure measurements were hindered by extremely low data rates so it is imperative to increase these rates for future experiments. This can be accomplished by improving the efficiency with which the Ps* atoms are detected [4,11], or by increasing the efficiency with which the Ps* atoms are formed. It was with the latter in mind that the present study of the Ps* formation fraction was undertaken. The formation fraction is defined as

$$f_2 = N_{\mathrm{Ps}*} / N_{e^+}, \tag{1}$$

where $N_{\mathrm{Ps}*}$ is the number of Ps* atoms produced and

N_{e^+} is the number of incident e^+.

Though the initial motivation for this experiment was simply to maximize f_2 for improved fine-structure measurements, it was discovered during the course of the investigation that measurements of f_2 are interesting in their own right. Two distinct energy populations have been observed in the Ps* spectra. This is consistent with similar observations in ground-state positronium [15]. Furthermore, the dependence of these two components upon the energy of the incident positrons may be interpreted in a manner consistent with theoretical studies of positronium formation and positron interactions in metals [16–18].

Measurements of f_2 have been performed for a variety of metal foils and crystals with no *in situ* surface treatment. No significant dependence of f_2 on sample material is observed—possibly due to the presence of an overlayer on all of the samples. However, the behavior of f_2 as a function of incident e^+ energy has been found to be of interest, as discussed below. Measurements of f_2 in a transmission geometry are discussed in the Appendix.

II. EXPERIMENTAL APPARATUS AND METHOD

The beam of slow positrons used in this experiment was produced with an electrostatic lensing system which has been described previously [19]. Slow positrons are produced by moderating β rays from a ^{22}Na source using tungsten vanes in a venetian-blind configuration [19]. Early data (on Mo foils) were taken using a 9-mCi source which yielded a maximum rate of 25 000 positrons per second on target. The beam was then upgraded and most of the data were taken with an 18-mCi source resulting in a maximum rate of 44 000 e^+ per second.

Evidence for the presence of Ps* atoms was obtained via the following decay chain:

$$2\,^3P_J \rightarrow \text{Lyman-}\alpha \text{ photon} + 1\,^3S_1$$
$$ \rightarrow 3\gamma. \tag{2}$$

Thus the signature for a Ps* event is a Lyman-α uv photon (243 nm) followed in delayed coincidence by an annihilation γ ray [5]. Note that only the $2\,^3P_J$ states may be detected in this manner. These states comprise 9 of the 16 sublevels within the $n=2$ shell.

The Lyman-α photons were detected with a solar-blind photomultiplier tube (PMT) with a 1.9-cm-diam photocathode (Hamamatsu model No. R821). This tube was custom-made with an especially thin quartz envelope to minimize scintillations caused by γ rays. The Lyman-α PMT was located inside the vacuum chamber to minimize interface transmission losses of the uv photons and eliminate γ-ray scintillations in the vacuum window. The annihilation γ rays were detected in a plastic scintillator (Pilot B) which was 10 cm in diameter and 10 cm long. A 5-cm-diam PMT (Amperex model No. XP2020) was attached to the scintillator. The signals from the Lyman-α and γ-ray detectors provided the start and stop, respectively, of a time spectrum collected with a time-to-amplitude converter and a multichannel analyzer. The geometry of the detection region is shown schematically in Fig. 1.

The Ps* formation fraction was measured for a variety of amorphous rolled-metal foils, an annealed polycrystalline molybdenum foil, and a nickel $\langle 111 \rangle$ single crystal. The incident energy of the positrons was controlled by adjusting a voltage applied directly to the sample. The measurements were made in a vacuum of $\sim 5 \times 10^{-8}$ Torr and no special preparation was performed on the samples other than ultrasonic cleaning.

Though there were no facilities for surface treatment and characterization *in situ,* Auger analysis was done in a separate surface analysis chamber before and after several runs. The surface contamination for all of the samples was dominated by $\sim 1-2$ monolayers of carbon— possibly hydrocarbons from the cleaning solvents. The significance of this surface layer is discussed below.
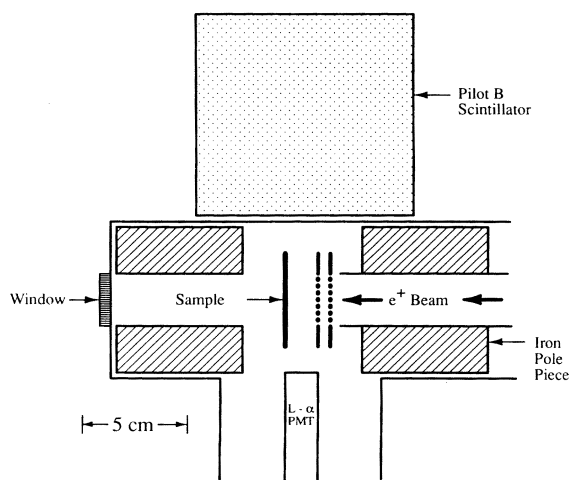
III. RESULTS AND ANALYSIS

The measured values of f_2 for all samples at 100-eV e^+ input energy are compared in Fig. 2(a). Despite the variety of target materials, there is no appreciable difference between the f_2 values displayed. In particular there is no trend with respect to the atomic number, electron density, or Ps* work function for the sample material. Similar consistency between samples was observed at all of the input energies investigated (10–1000 eV). This consistency may be due to the similarity between the surfaces as a result of the contamination . The behavior of f_2 as a function of e^+ input energy is displayed in Fig. 3(a). Each of the points in Fig. 3(a) represents the weighted average of f_2 values measured on all available samples at the given incident energy. Some of the samples were not measured at every energy. The maximum measured value of the total formation fraction is $f_2 = (2.05 \pm 0.22) \times 10^{-2}$, where the quoted error is purely statistical. This value is the same for all of the samples studied and remains constant from 10–100-eV e^+ input energy. There is a systematic error in this number of 0.44×10^{-2}, as discussed below.

In order to study the shape of the timing spectra with reasonably good statistics, data from the different samples were summed. Spectra from all samples and energies with appreciable signals (10–200 eV) were included. The resulting grand sum spectrum is shown in Fig. 4.

FIG. 1. Schematic of the detection region. The grids used are 90% open-area (20 lines per cm copper). The iron pole pieces are present to provide a uniform magnetic field for other experiments. They were de-Gaussed for the present work.
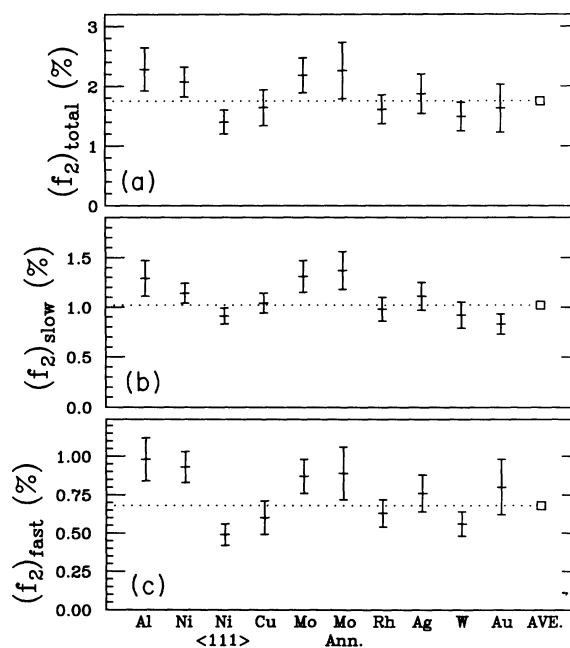
FIG. 2. Comparison of target materials. Measured values of f_2 are compared for each of the samples investigated at 100-eV e^+ input energy. The data are plotted in order of increasing Z. The total formation fraction is displayed in (a). The formation fraction in the long-lifetime component is shown in (b), and (c) displays data on the short-lifetime component. No trends are apparent, and all of the data are reasonably consistent with the weighted averages (box symbols on the right).
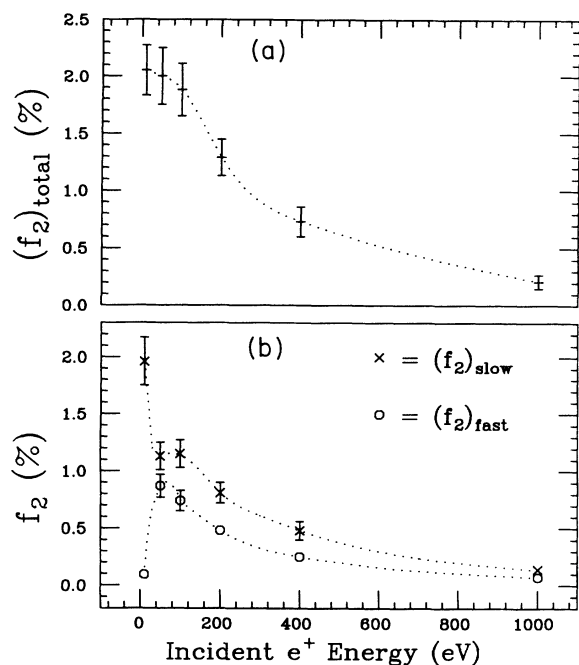
FIG. 3. Formation fraction versus positron input energy. The data for all of the samples are summed and the behavior of f_2 with respect to incident e^+ energy is displayed. The total formation fraction is shown in (a). The two lifetime components are shown separately in (b). The dotted lines are smooth curves plotted to guide the eye. The plotting symbols serve as error bars for those points which lack them. Note the disappearance of the fast component at low energy and the corresponding augmentation of the slow component.
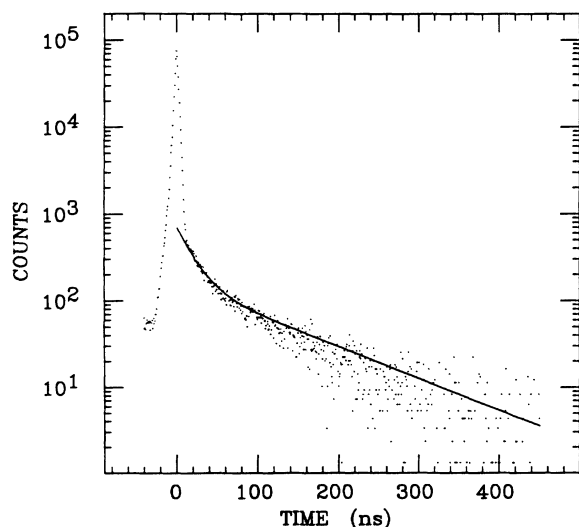
FIG. 4. Ps* time spectrum. Data from all samples and energies from 10–200 eV were summed in order to study the shape of the spectrum. These data were fit to the sum of two exponential components. The solid curve represents the fit. A flat background has been subtracted from this spectrum. The background level may be seen at negative times.

The "prompt" peak at $t = 0$ in Fig. 4 is due to simultaneous γ-ray scintillations in the Lyman-α PMT and in the plastic γ-ray detector. It is clear that the data for $t > 0$ do not represent the simple exponential decay of o-Ps formed via the decay chain shown in Eq. (2). Fortunately, the data may be successfully characterized by the sum of two exponentials with markedly different decay rates. The fitting was done with a five-parameter maximum-likelihood routine [20]. The five parameters were the decay rates and intensities of each of the two exponential components plus a background. The results for the two lifetimes were 113.3 ± 6.7 ns for the long-lifetime component and 18.5 ± 1.7 ns for the short-lifetime component.

Using these parameters as guidelines the fitting routine was applied to individual spectra and the behavior of each of the components was studied. The lifetimes obtained for the individual spectra (both components) were consistent with the values given above for the summed spectrum. Formation fractions are defined individually for each component. The probability (per incident e^+) of forming Ps* in the long-lifetime component is given by $(f_2)_{\text{slow}}$, while $(f_2)_{\text{fast}}$ represents the probability of forming Ps* in the short-lifetime component. The "slow" and "fast" subscripts refer to the average velocity of the Ps* atoms in each component as well as the observed lifetime (see Sec. V).

The material dependence of $(f_2)_{\text{slow}}$ and $(f_2)_{\text{fast}}$ is shown in Figs. 2(b) and 2(c), respectively. There are no significant variations from sample to sample in either component. By summing the data for all targets at each incident e^+ energy, the energy dependence of the two components was studied [as shown in Fig. 3(b)]. The significant difference in energy dependence between the two components is discussed below.

The formation fraction is calculated as follows:

$$f_2 = \frac{16}{9} \frac{r}{C_{\text{ref}}\eta_\alpha\eta_d\eta_\gamma B} , \tag{3}$$

where r is the detected rate of Ps* events, C_{ref} accounts for reflections of Lyman-α photons from the sample, η_α includes the solid angle of the Lyman-α detector and its quantum efficiency, η_d accounts for losses in the Lyman-α discriminator, η_γ is the efficiency of the γ-ray detector, and B is the e^+ beam rate. The factor of $\frac{16}{9}$ arises from the assumption that all 16 $n = 2$ sublevels are equally populated and the fact that only the nine $2\,^3P_J$ states are detected.

The detected Ps* rate (r) is an integrated intensity of o-Ps counts in a time spectrum (obtained from the maximum-likelihood routine) divided by a run duration. In calculating $(f_2)_{\text{slow}}$ the intensity of the long-lifetime component is used. Likewise the intensity of the short-lifetime component yields $(f_2)_{\text{fast}}$. The sum of these intensities produces f_2.

The total Lyman-α detection efficiency has three contributions. The first (C_{ref}) takes into account the enhancement of the uv light collection if the sample acts as a partial mirror. This effect is discussed in detail in Sec. IV.

The second contribution to the Lyman-α detection efficiency (η_a) is simply the efficiency of the PMT. This includes quantum efficiency and solid angle. The quantum efficiency of the Lyman-α PMT is the only factor in Eq. (3) which was not measured or calculated. It is taken to be 11% from data published by the manufacturer. A large instrumental uncertainty ($\sim 20\%$) is assigned to this number since the quantum efficiency of PMT's is known to vary significantly from tube to tube. The solid angle of the Lyman-α PMT can be determined accurately due to the very straightforward detection geometry used (see Fig. 1). The solid angle is $\sim 1\%$, which yields a value of $\eta_a = (1.1 \pm 0.2) \times 10^{-3}$.

The third contribution (η_d) accounts for losses of real Lyman-α events in the discriminator used to remove electronic noise. A Monte Carlo simulation of the PMT pulse-high distribution was used to determine η_d. The secondary emission of electrons from the dynodes was assumed to follow a Poisson distribution. The results of this simulation can be seen in Fig. 5. The value of η_d is determined by taking the ratio of the measured count rate at 50 mV (where the data were taken) to the count rate at 0 mV given by the simulation. This yields a value of $\eta_d = 0.571 \pm 0.023$. The error in this number is chosen to encompass a lower limit on η_d of 0.548 determined by a linear extrapolation to the data in Fig. 5.

The efficiency of the γ-ray detector (η_γ) and the incident e^+ beam rate (B) were measured by replacing the sample with a channel electron multiplier array (CEMA) assembly. This assembly included a phosphor screen which permitted visual inspection of the beam profile.
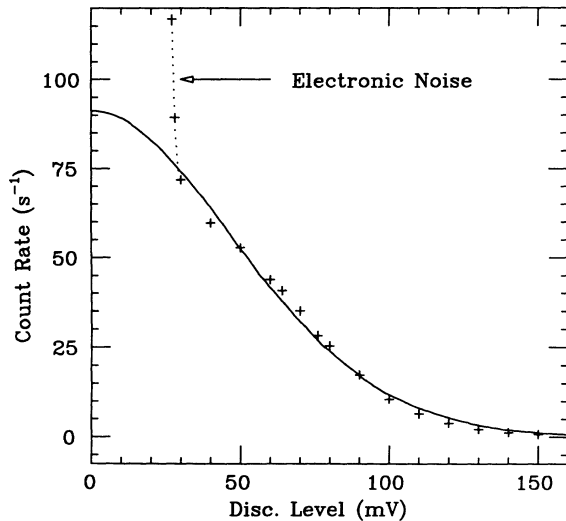
FIG. 5. Discriminator curve for determining η_d. The crosses represent discriminator curve data taken by leaking light into the vacuum system. The curve is the result of a Monte Carlo simulation which assumed Poisson statistics for the emission of secondary electrons. It has been scaled to match the data (both axes). No plateau is evident due to the lack of a high-gain first dynode in the PMT. The value of η_d is taken to be the ratio of the 50-mV data point to the 0-mV value of the simulation.

Given the background-corrected rates of the CEMA (R_{start}), the γ-ray detector (R_{stop}), and of coincidence events (R_{coin}), η_γ and B are found as follows:

$$\eta_\gamma = \frac{R_{\text{coin}}}{R_{\text{start}}}, \quad B = \frac{R_{\text{start}} R_{\text{stop}}}{R_{coin}}. \tag{4}$$

These quantities were monitored infrequently due to the inconvenience of installing the CEMA assembly. However, B remained constant within $\pm 10\%$ over time scales of many months and η_γ was stable at 0.105 ± 0.005. It should be noted that the errors quoted above for η_a, η_d, and η_γ are instrumental uncertainties which contribute a systematic error of 22% to the absolute determination of any f_2 value, but do not contribute to relative comparisons of f_2 values as in Figs. 2 and 3.

IV. SYSTEMATICS

The Ps* signature [Eq. (2)] is difficult to mimic with non-Ps* events. However, since the shape of the prompt peak is not known a priori, it is possible that there is significant contamination of the Ps* signal from "prompt" γ-ray coincidences. This possibility was tested by placing aluminum foil over the Lyman-α detector, which eliminated true Ps* events without blocking any γ rays. There was no detectable Ps* signal with this foil in place.

Another event which would produce a false signal is a scintillation in the sample caused by the impact of a positron followed by an annihilation γ ray from positronium formed with the same positron. The wavelength of the light which gives rise to the start signal has been measured using an interference filter in an experimental arrangement similar to the present one [21]. The wavelength was found to be 246 ± 3 nm, as opposed to the broad range expected from a scintillation event. Furthermore, surface scintillations become more common and intense as the e^+ input energy increases. Thus the disappearance of the signal at high input energy (see Fig. 3) indicates that the detected signal is due to Ps*.

There is a systematic effect in the measurement of the γ-ray detection efficiency. This is because 95% of the γ rays used to determine η_γ via Eq. (4) were the result of 2γ prompt annihilations whereas the detected Ps* events were due primarily to 3γ o-Ps decays. The detection efficiencies for these two types of events are not the same due to phase-space considerations and the different γ-ray energies involved. This difference has been measured to be $\sim 7\%$ for Pilot B scintillator used in a geometry similar to that of the present experiment [22]. Thus, the maximum systematic uncertainty in η_γ is taken to be 7%.

At low input energy there is a considerable systematic effect due to the sample acting as a lensing element in the electrostatic beam. This effect was investigated by replacing the sample with a grid backed by the CEMA detector assembly. The grid consisted of a 3-mm-thick ring with 87% open-area Ni mesh (28 lines per cm) mounted on both sides. This double mesh provided high positron transmission coupled with low penetration of electric field from the CEMA. The beam rate was then

measured as a function of the voltage applied to the grid. The curve obtained in this manner (beam rate vs grid voltage) was used to correct the maximum (high voltage) beam rate and find the proper beam rate for each run. The maximum beam rate was monitored between series of tests on several samples. The correction was less than 5% for all of the data except the very lowest input energy (10 eV) where it was 36%.

The effective solid angle of the Lyman-α PMT was systematically increased by reflections from the sample. This was accounted for by C_{ref} in Eq. (3). The expected form for this factor is $C_{\text{ref}} = 1 + \mathcal{R}$, where $\mathcal{R}$ is the reflectivity of the sample at 243 nm. This is reasonable because the $2\,^3P_J$ states are short-lived (~ 3 ns) and therefore always decay close to the surface. Thus the solid angle for the reflected image is virtually the same as that of the emitting Ps* atom, and the intensity of the image is just $\mathcal{R}$ times the full intensity. This argument applies similarly to specular or diffuse reflection. A search of the literature provided uv reflectivities for the samples studied [23–30]. However, most of the published reflectivity measurements employed clean, evaporated films rather than untreated foils.

This motivated an experiment to measure C_{ref} directly for the foils used in the present work. In this experiment the Lyman-α PMT and the foil samples were placed inside a light-tight box with the same relative positions as in Fig. 1. A 1-mm quartz uv lightguide was inserted through the wall of the box. The tip of the lightguide, which was rounded and roughened for isotropic emission, was placed ~ 1 mm from the sample. This distance roughly corresponds to the mean distance traveled by the $2\,^3P_J$ atoms during their 3-ns lifetime. A mercury discharge lamp outside the box provided uv radiation. An interference filter centered on 250 nm was placed over the PMT. The value of C_{ref} was taken to be the ratio of the PMT count rate with the sample in place to the count rate with the sample removed (after subtracting background counts). There was a systematic problem with this experiment due to the anisotropic output of the uv lightguide. For this reason the measured values of C_{ref} are given less weight in the analysis.

The results of these two investigations of C_{ref} are shown in Table I. The errors attributed to most of the measured values represent the statistical spread of many independent measurements. However, the Ni and Ag samples were measured only once. These samples were therefore assigned an artificial but conservative 10% error. The error values used in the analysis were chosen to cover the spread in the published numbers—with two notable exceptions. First, the spread in the literature values for Al represents a single study of the reflectivity as a function of sample preparation. This prompted the use of the measured value of C_{ref} for Al, which is justified by the good agreement between the measurements and the published values for the other samples. Second, the lower value for tungsten [26] has been largely discounted after studying the details of the two measurements. Samples without several comparable values (Al, Mo, Rh, and W) have been assigned an error of 10%. For the data in Fig. 3, where runs on several different samples were summed, average values of C_{ref} were found at each energy using the values in Table I weighted by the beam rates and durations of the runs in the sum.

Finally, as a test of reproducibility, the 100-eV measurement on Mo was repeated several times—both before and after the beam upgrade mentioned in Sec. II. Though the beam rate and the details of the e^+ lensing changed significantly, consistent results were obtained.

V. DISCUSSION

Three features of the Ps* data presented above merit discussion: the observation of two components in the time spectrum (Fig. 4), the lack of material dependence of f_2 (Fig. 2), and the generally high values of f_2 (Fig. 3). The presence of the two components is a result of the limitations of the apparatus. Ideally, the Ps* (and subsequent o-Ps) would be completely isolated and detected with a constant efficiency. Under these conditions, the o-Ps resulting from the decay process of Eq. (2) would exhibit simple exponential decay with its vacuum annihilation lifetime (142 ns [13,14]). However, in the present experiment the o-Ps is exposed to an environment which is far from ideal both because of a lack of total isolation and because of a spatially dependent detection efficiency. The resulting complicated time spectrum provides information about the Ps* formation process which would be unavailable in the ideal case.

There are two major effects which can alter the o-Ps

TABLE I. Determination of C_{ref}. The "literature" column represents the spread in values from several different sources.

Sample	$1 + \mathcal{R}$ (Literature)	C_{ref} (Measured)	C_{ref} (For analysis)	References
Al	1.15–1.92	1.58±0.04	1.58±0.16	30
Ni	1.35–1.47	1.43±0.14	1.41±0.06	23,26,28
Cu	1.25–1.39	1.30±0.02	1.32±0.07	23,25,26,30
Mo	1.25	1.29±0.02	1.25±0.13	26
Rh	1.64	1.55±0.11	1.64±0.16	30
Ag	1.18–1.34	1.25±0.13	1.26±0.08	23,24,25,26,28,30
W	1.16, 1.54		1.50±0.15	26,29
Au	1.24–1.39		1.32±0.07	23,25,26,30
C	1.17–1.19		1.18±0.01	26,27

lifetime: collisional quenching and disappearance [14]. Collisional quenching is the 2γ annihilation of o-Ps upon interaction with any surface inside the vacuum chamber. Disappearance is the removal of o-Ps events from the time spectrum due to o-Ps atoms traveling into a region of low detection efficiency before decaying. This effect gives rise to a systematic underestimate of the amount of Ps* present, as discussed below.

Both collisional quenching and disappearance systematically reduce the observed o-Ps lifetime and both depend on the kinetic energy of the o-Ps. Since the momentum transferred during Lyman-α emission is negligible, the kinetic energy of the resulting o-Ps is essentially equal to the kinetic energy of the Ps* (K^*). This energy is given by

$$K^* = K - \phi_+ - \phi_- + 1.7 \text{ eV} , \tag{5}$$

where ϕ_+ (ϕ_-) is the positron (electron) work function for the metal, K is the kinetic energy of the positron in the metal as it reaches the surface, and 1.7 eV is the binding energy of Ps*.

Collisional quenching is a dominant effect for $K^* \gtrsim 6.8$ eV (the o-Ps ionization potential). At such energies the o-Ps will most likely be ionized upon the first wall collision resulting in an almost immediate annihilation of the freed positron. Thus the decay of o-Ps for $K^* \gtrsim 6.8$ eV is not expected to be purely exponential. The measured lifetime of energetic o-Ps is governed by the transit time required to collide with the nearest surface. This transit time is given by

$$t = \frac{d}{\sqrt{K^*/m_e}} - \tau_\alpha , \tag{6}$$

where d is the mean distance from the target to any surface (~ 5 cm), $\tau_\alpha = 3.2$ ns is the Lyman-α decay lifetime, and m_e is the electron mass. If $K^* < 6.8$ eV then the probability of collisional quenching drops sharply and the o-Ps atoms typically experience hundreds of wall collisions [14] before 2γ annihilation occurs. As a result, energetic positronium is expected to exhibit a much shorter measured lifetime than slow positronium.

The long-lifetime ("slow") component in Fig. 4 presumably arises from Ps* with $K^* < 6.8$ eV. This identification is supported by a measurement [8] of $K^* \approx 2$ eV for positronium in the $2\,{}^3S_1$ state using a detection scheme which was effectively sensitive only to the slow component. In the same measurement, the observed ratio of the $2\,{}^3S_1$ formation rate to that of the $2\,{}^3P_J$ states was consistent with the assumption of equal population for all magnetic sublevels. This supports the use of the factor $\frac{16}{9}$ in Eq. (3).

The short-lifetime ("fast") component is attributed to Ps* with $6.8 < K^* < 60$ eV. The lifetime of this component (18.5 ns) corresponds to $K^* \approx 30$ eV [from Eq. (6)]. This is interpreted as the average energy of the Ps* in the fast component, but the energy spread is expected to be tens of eV. A search for Ps* above 60 eV yielded null results; no signal comparable in amplitude to the fast component was observed for lifetimes between 4 and 12 ns (corresponding to 300 and 60 eV, respectively).

Searches above 300 eV were precluded by the prompt peak resolution.

Two populations of Ps* have been observed: one with a mean energy of several eV and one with several tens of eV. The Ps* energy distribution is governed by the Ps* formation cross section [$\sigma(K)$] and details of the energy distribution of positrons near the surface [$n(K)$]. If the origin of the two components is to be understood, then a more careful consideration of these factors is required.

It is usually assumed [15,31] that $\sigma(K)$ is proportional to $1/K$ for K well above the threshold value implied by Eq. (5),

$$K_{\text{thr}} = \phi_+ + \phi_- - 1.7 \text{ eV} . \tag{7}$$

This assumption has been used to produce the schematic representation of $\sigma(K)$ shown in Fig. 6(b). Figure 6(c) displays a suggestive sketch of $n(K)$ which highlights three prominent features: (1) thermalized positrons [32], (2) epithermal positrons [32], and (3) backscatter positrons [17]. The relative proportions of the three components are not necessarily to scale.
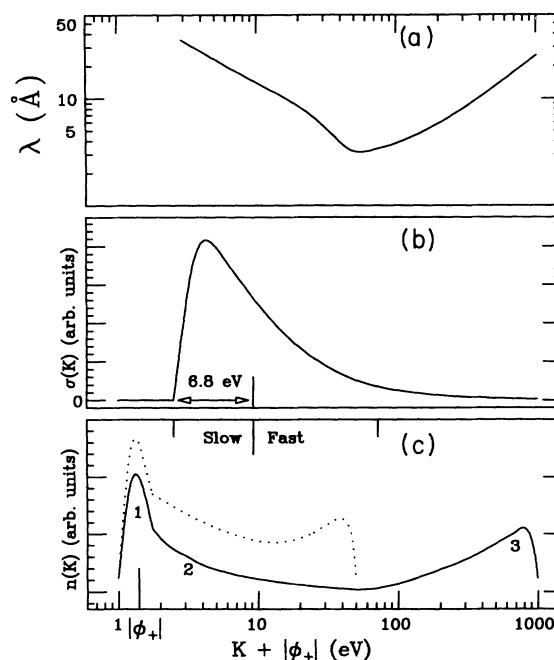

FIG. 6. Effect of e^+ energy on Ps* formation. The calculated energy dependence of the positron scattering length is shown in (a) as redrawn from Ref. [16] (calculated for Al). In (b), a schematic shape for the Ps* formation cross section [$\sigma(K)$] is proposed based on Refs. [15] and [31]. The general shape of the number density of e^+ near the surface [$n(K)$] is sketched in (c). The solid curve represents $K_{\text{inc}} = 1$ keV, while the dotted curve is for $K_{\text{inc}} = 50$ eV. The three components of $n(K)$ shown in this figure are (1) thermalized positrons (based on Ref. [32]), (2) epithermal positrons (also based on Ref. [32]), and (3) backscatter positrons (based on Ref. [17]). The energy regimes attributed to the fast and slow components are demarcated at the top of (c). The energy of positrons just below the surface is plotted on the x axis. It has been offset (by the positron work function) for plotting purposes.

Positrons that have thermalized in the metal can diffuse to the surface over long distances (hundreds of Å in an annealed metal crystal). However, the presence of thermalized positrons at the surface does not imply copious Ps* formation. The threshold for Ps* formation [Eq. (7)] implies that only the Boltzmann tail of the thermal positron distribution is energetic enough to yield Ps*. Direct evidence precluding significant Ps* production from thermalized positrons is obtained from the small value of $(f_2)_{slow}$ at large incident positron energies (K_{inc}). This is especially true for the Ni crystal and the annealed Mo since thermalized positrons were observed to be abundantly reemitted from these two samples at $K_{inc} \approx 1$ keV. However, few of these thermalized positrons were converted to Ps*.

Epithermal positrons are those that reach the surface of the metal with energies of a few eV. The shape of the epithermal distribution is governed by the scattering length curve, which is shown in Fig. 6(a). The minimum scattering length is ~ 3 Å in most metals and occurs between 30 and 70 eV for the metals used in this study [33]. For $K < 30$ eV any loss of energy due to scattering results in a larger scattering length and thus a greater escape probability. As K_{inc} increases above ~ 70 eV, positrons are implanted deeper and any energy loss decreases the scattering length [see Fig. 6(a)]. Thus it is relatively unlikely that positrons with $K_{inc} > 70$ eV will return to the surface at epithermal energies.

The backscatter component consists of positrons that are sent back through the surface after one or two large-angle scatters so that K peaks at a large fraction of K_{inc}. Monte Carlo calculations [17] indicate that for $K_{inc} = 2$ keV the backscatter energy peaks at $K/K_{inc} \approx 0.95$. No calculations have yet been carried out at lower incident energies, but the trend of these results indicates that similar peaking near the incident energy is expected. Thus positrons at all energies less than K_{inc} are found exiting the sample. As K_{inc} is decreased, an increasing fraction of the backscattered positrons fall in the range of K attributed to the fast component [as shown for $K_{inc} = 50$ eV in Fig. 6(c)]. At $K_{inc} = 10$ eV the backscatter peak should fall in the range of 6–9 eV and effectively form only slow-component Ps* with $K^* < 6.8$ eV. The above description is supported by the energy dependence of $(f_2)_{slow}$ and $(f_2)_{fast}$ shown in Fig. 3(b), but it must be noted that the surface overlayer may play a roll—particularly at low energy.

For K_{inc} in the range of tens to hundreds of eV, Ps* formation in the slow component is predominantly derived from epithermal positrons, while the fast component is primarily due to backscatter positrons. When K_{inc} drops into the eV range, both epithermal and backscatter positrons contribute to the slow component and the fast component virtually disappears. Thermalized positrons never contribute significantly to Ps* formation because of the energy threshold of Eq. (7) [see Figs. 6(b) and 6(c)].

The absence of material dependence demonstrated in Fig. 2 is unexpected. There may be a small amount of nonstatistical scatter in these data; however, no trends

are apparent with respect to several material properties. The Ps* formation process is constrained by Eq. (7) at low K and thus some dependence on the work function might be expected in this regime. Any such work-function dependence may have been eliminated by the significant surface contamination. The scattering-length curve affects the production of epithermal positrons (and hence Ps*), and this curve is a function of material. However, the value of the minimum scattering length and the shape of the scattering-length curve are similar for different metals. The major material-dependent effect is a change in the energy at which the minimum occurs; effectively sliding the curve in Fig. 6(a) from left to right. Such a subtle change may be undetectable at the present level of precision. In the ~ 10-keV energy range, the positron backscatter has a significant Z dependence [18]. Similar dependence could be expected here but is not seen, perhaps indicating a different Z dependence at low e^+ input energy.

The most startling aspect of the results presented here is the large size of f_2 for incident energies up to 100 eV. Such a large f_2 is not a priori impossible. Formation of $n = 2$ positronium in H_2 gas [34] has yielded $f_2 = 6\%$. Furthermore, calculations of positronium formation in atomic hydrogen [31] indicate that the formation fraction of n-level positronium (f_n) is roughly proportional to $1/n^2$ or $1/n^3$. Values of f_1 are typically 20%–50% for metal targets—even for epithermal positrons [15]. Thus, $f_2 \approx 2\%$ is not unreasonable.

However, in previous experiments [5,6,21] the observed formation fractions were significantly smaller. In particular, f_2 was previously measured to be $\sim 0.4\%$ for cleaned and characterized W and Cu surfaces under UHV conditions [6]. The discrepancy between these UHV results and the non-UHV measurements presented here could be attributed to the presence of 1-2 monolayers of carbon or hydrocarbons found on the present samples. Since the electron density is too high for positronium formation in the bulk of metals, it is assumed that a positron can only form Ps* with an electron from the tail of the metal electron distribution or from any surface contamination. A carbon or hydrocarbon surface layer would probably have a sufficiently low electron density to allow Ps* formation within a volume greater than the small formation volume available at the surface of cleaned samples. While this explanation is plausible, no evidence that clean surfaces have smaller $n = 2$ formation fractions is observed when the same apparatus is used to measure f_2 under both UHV and non-UHV conditions [6].

Finally, it should be noted that the values of f_2 reported here must be considered lower limits for two reasons. The first reason has to do with the use of manufacturer's specifications to determine η_α. Such specifications are notoriously unreliable. However, actual quantum efficiencies virtually never exceed specifications by more than 20% so an overestimate of η_α is more likely than an underestimate. Therefore, it is more probable to measure a systematically low result for f_2 than a systematically high result.

The second reason that the present measurements are lower limits is the effect of disappearance. When collisional quenching occurs the annihilation γ ray may still be detected. Thus, though the lifetime is decreased by quenching, the integrated intensity of the spectrum is unchanged. Disappearance, on the other hand, is a result of o-Ps leaving the detection region and decaying undetected. Thus, disappearance causes a systematic underestimate of the amount of positronium present.

In the present apparatus disappearance should only be appreciable for o-Ps atoms which enter the iron pole piece (see Fig. 1) which is an effective γ-ray shield. A simple solid angle calculation indicates that only $\sim 10\%$ of the atoms in the fast component are expected to disappear in this manner. Solid angle considerations are insufficient for the slow component due to the possibility of multiple wall collisions. The slow-component lifetime (113 ns) is $\sim 20\%$ lower than the vacuum o-Ps lifetime. Thus there is an absolute upper limit of 20% on the disappearance effect for this component. Studies of o-Ps confined in cavities [14] indicate that the expected disappearance for the present geometry is $\sim 10\%$. Thus, the actual values of f_2 (both components) are perhaps $\sim 10\%$ greater than the measured values reported here.

ACKNOWLEDGMENTS

APPENDIX

All of the data presented above were collected in a reflection geometry, i.e, the Ps* atoms were emitted from the same side of the target into which the positrons were implanted. However, design considerations for the proposed Ps* fine-structure measurement [11] favor a transmission geometry for Ps* formation. For this reason a survey of f_2 for a variety of transmission samples was undertaken. The results are summarized below.

Two types of samples were investigated: foils and meshes. The foils are truly transmission samples in that the positrons pass through the material of the sample. The meshes, on the other hand, employ a transmission geometry but the formation of Ps* presumably occurs as a result of glancing-angle reflections from the mesh wires.

The experimental geometry used in the transmission tests was very similar to that of the reflection tests. The major difference was that the sample and the last grid of the e^+ beam were interchanged (see Fig. 1). Due to the symmetry of the detection region this change had no effect upon any of the detection efficiencies.

The individual transmission time spectra could not be analyzed in the same manner as the reflection spectra because of the smaller count rates involved. Data from all of the transmission samples were summed to study the spectrum shape. This sum spectrum was fit with the above-mentioned five-parameter fitting routine and the lifetimes obtained were consistent with those measured for the reflection data. In order to analyze individual data runs it was assumed that all of the spectra contained two components with the same lifetimes and same ratio of intensities as the summed (transmission) spectrum. With this assumption it was possible to convert a count rate in a time window (from 25 to 100 ns) into a Ps* rate for use in Eq. (3). All other factors in the analysis were the same as the reflection tests except that the C_{ref} values for the meshes were corrected for open area.

The mesh samples studied were a 66% open-area monel mesh, a 49% open-area Mo mesh, and the same Mo mesh fumed with MgO. The foils studied were a thin, homemade VYNS (a polyvinylchloride-acetate copolymer) foil [35], the same VYNS foil with an evaporated layer of Au, and a commercially obtained C foil (32 nm thick). Thickness measurements of the homemade foils are not available. The foils were mounted on 95% open-area Cu grids (8 lines per cm) with the grid on the e^+ input side.

As with the reflection data, the values of f_2 measured in the transmission geometry were studied as a function of the incident e^+ beam energy. The maximum values of f_2 obtained in this geometry are listed in Table II. The relationship between beam energy and f_2 for the mesh samples should be similar to that observed for positronium formation in a glancing-angle geometry [36]. However, since the details of positron transmission through foils are not known, the relationship between the e^+ beam energy and f_2 is unclear for the foil samples—particularly

TABLE II. Summary of Ps* formation in a transmission geometry. The f_2 values listed are the maximum obtained for each sample.

Sample	$10^3 f_2$	e^+ beam energy (eV)
Mo mesh	7.0 ± 0.9	100
Monel mesh	5.8 ± 0.9	100
Mo mesh with MgO	0.5 ± 0.4	100
VYNS foil with Au	1.9 ± 0.3	2000
VYNS foil	1.4 ± 0.4	1275
C foil	1.1 ± 0.3	1700

those for which the thickness is not known. Measurements of the transmitted beam rate versus beam energy yielded typical "S-shaped" curves for the foil samples. For each of the samples, the maximum transmission plateau was reached at a beam energy ~ 1.2 times the energy for maximum f_2 (listed in Table II). This ratio should remain fairly constant for any foil thickness even though the absolute beam energy for maximum f_2 depends strongly on the thickness of the foil. Thinner foils would

presumably improve the Ps* yield.

The maximum glancing-angle Ps formation fractions reported [36] were in the range of 3–5 %. The present value for the meshes ($f_2 \approx 0.6\%$) is consistent with the $f_n \propto \sim 1/n^3$ dependence discussed in Sec. V. This indicates that the formation of Ps* both in transmission through meshes and in reflection from foils is probably governed by similar effects.

[1] K. P. Ziock, R. H. Howell, F. Magnotta, R. A. Failor, and K. M. Jones, Phys. Rev. Lett. 64, 2366 (1990).

[2] S. L. Varghese, E. S. Ensberg, V. W. Hughes, and I. Lindgren, Phys. Lett. 49A, 415 (1974).

[3] S. Chu and A. P. Mills, Jr., Phys. Rev. Lett. 8, 1333 (1982).

[4] M. S. Fee, A. P. Mills, Jr., E. D. Shaw, R. J. Chichester, D. M. Zuckerman, S. Chu, and K. Danzmann, Phys. Rev. A 44, R5 (1991).

[5] K. F. Canter, A. P. Mills, Jr., and S. Berko, Phys. Rev. Lett. 34, 177 (1975).

[6] D. C. Schoepf, S. Berko, K. F. Canter, and A. H. Weiss, in Positron Annihilation, edited by P. G. Coleman, S. C. Sharma, and L. M. Diana (North-Holland, New York, 1982), p. 165.

[7] A. P. Mills, Jr., S. Berko, and K. F. Canter, Phys. Rev. Lett. 34, 1541 (1975).

[8] S. Hatamian, R. S. Conti, and A. Rich, Phys. Rev. Lett. 58, 1833 (1987).

[9] R. Ley, K. D. Niebling, R. Schwarz, and G. Werth, J. Phys. B 23, 1915 (1990).

[10] T. Fulton and P. C. Martin, Phys. Rev. 95, 811 (1954).

[11] T. D. Steiger, B. Ghaffari, A. Rich, and R. S. Conti, Abstracts of Contributed Papers, 12th International Conference on Atomic Physics, Ann Arbor, 1990, edited by W. E. Baylis, G. W. F. Drake, and J. M. McConkey (Department of Physics, University of Windsor, Windsor, Ontario, 1990), p. I-22.

[12] R. N. Fell, Ph.D. thesis, Brandeis University, 1990; Phys. Rev. Lett. 68, 25 (1992).

[13] C. I. Westbrook, D. W. Gidley, R. S. Conti, and A. Rich, Phys. Rev. A 40, 5489 (1989).

[14] J. S. Nico, D. W. Gidley, A. Rich, and P. W. Zitzewitz, Phys. Rev. Lett. 65, 1344 (1990).

[15] R. H. Howell, I. J. Rosenberg, and M. J. Fluss, Phys. Rev. B 34, 3069 (1986).

[16] R. M. Nieminen and J. Oliva, Phys. Rev. B 22, 2226 (1980).

[17] S. Valkealahti and R. M. Nieminen, Appl. Phys. A 32, 95 (1983).

[18] S. Valkealahti and R. M. Nieminen, Appl. Phys. A 35, 51 (1984).

[19] J. Van House and P. W. Zitzewitz, Phys. Rev. A 29, 96 (1984).

[20] P. H. R. Orth, W. R. Falk, and G. Jones, Nucl. Instrum. Methods 65, 301 (1968).

[21] S. Hatamian, Ph.D. thesis, University of Michigan, 1987.

[22] G. Gerber, D. Newman, A. Rich, and E. Sweetman, Phys. Rev. D 15, 1189 (1977).

[23] E. Hagen and H. Rubens, Ann. Phys. (Leipzig) 8, 1 (1902).

[24] R. S. Minor, Ann. Phys. (Leipzig) 10, 581 (1903).

[25] W. W. Coblentz, Natl. Bur. Stand. Bull. 5, 339 (1908).

[26] E. O. Hulburt, Astrophys. J. 42, 205 (1915).

[27] W. W. Coblentz and C. W. Hughes, Natl. Bur. Stand. Sci. Papers 19, 577 (1924).

[28] W. W. Coblentz and R. Stair, Natl. Bur. Stand. J. Res. 2, 343 (1929).

[29] H. C. Hamaker, Reflectivity and Emissivity of Tungsten (North-Holland, Amsterdam, 1934).

[30] G. Hass, J. Opt. Soc. Am. 45, 945 (1955).

[31] H. S. W. Massey and C. B. O. Mohr, Proc. Phys. Soc. A 67, 695 (1954).

[32] D. A. Fischer, K. G. Lynn, and D. W. Gidley, Phys. Rev. B 33, 4479 (1986).

[33] D. R. Penn, Phys. Rev. B 13, 5248 (1976).

[34] G. Laricchia, M. Charlton, G. Clark, and T. C. Griffith, Phys. Lett. 109A, 97 (1985).

[35] D. W. Green, J. Sci. Instrum. 38, 333 (1961).

[36] D. W. Gidley, R. Mayer, W. E. Frieze, and K. G. Lynn, Phys. Rev. Lett. 58, 595 (1987).
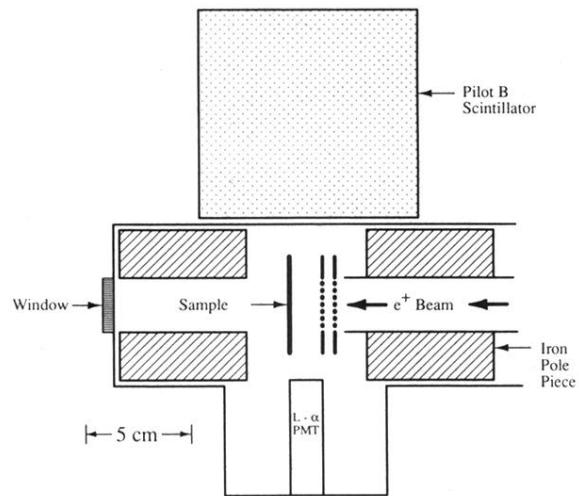
FIG. 1. Schematic of the detection region. The grids used are 90% open-area (20 lines per cm copper). The iron pole pieces are present to provide a uniform magnetic field for other experiments. They were de-Gaussed for the present work.